Inertial migrations of cylindrical particles in rectangular microchannels: Variations of equilibrium positions and equivalent diameters

Jinghong Su, Xiaodong Chen, and Guoqing Hu

Citation: Physics of Fluids **30**, 032007 (2018); doi: 10.1063/1.5018714
View online: https://doi.org/10.1063/1.5018714
View Table of Contents: http://aip.scitation.org/toc/phf/30/3
Published by the American Institute of Physics

Inertial migrations of cylindrical particles in rectangular microchannels: Variations of equilibrium positions and equivalent diameters

Jinghong Su,[1,2] Xiaodong Chen,[1,2,a)] and Guoqing Hu[1,2,a)]
[1]*The State Key Laboratory of Nonlinear Mechanics (LNM), Institute of Mechanics, Chinese Academy of Sciences, Beijing 100190, China*
[2]*School of Engineering Science, University of Chinese Academy of Sciences, Beijing 100049, China*

(Received 8 December 2017; accepted 2 March 2018; published online 22 March 2018)

Inertial migration has emerged as an efficient tool for manipulating both biological and engineered particles that commonly exist with non-spherical shapes in microfluidic devices. There have been numerous studies on the inertial migration of spherical particles, whereas the non-spherical particles are still largely unexplored. Here, we conduct three-dimensional direct numerical simulations to study the inertial migration of rigid cylindrical particles in rectangular microchannels with different width/height ratios under the channel Reynolds numbers (Re) varying from 50 to 400. Cylindrical particles with different length/diameter ratios and blockage ratios are also concerned. Distributions of surface force with the change of rotation angle show that surface stresses acting on the particle end near the wall are the major contributors to the particle rotation. We obtain lift forces experienced by cylindrical particles at different lateral positions on cross sections of two types of microchannels at various Re. It is found that there are always four stable equilibrium positions on the cross section of a square channel, while the stable positions are two or four in a rectangular channel, depending on Re. By comparing the equilibrium positions of cylindrical particles and spherical particles, we demonstrate that the equivalent diameter of cylindrical particles monotonously increases with Re. Our work indicates the influence of a non-spherical shape on the inertial migration and can be useful for the precise manipulation of non-spherical particles. *Published by AIP Publishing.*
https://doi.org/10.1063/1.5018714

I. INTRODUCTION

Microfluidics emerges as promising technologies for manipulation and detection of particles or cells. Different active methods resorting to external fields for particle focusing or separation have been developed, e.g., dielectrophoresis,[1–3] acoustophoresis,[4,5] magnetophoresis,[6,7] and thermophoresis.[8,9] Recently, inertial migration has been widely used for focusing,[10–13] separation,[14–18] filtration,[18,19] enrichment,[16,20] or hydrodynamic stretching of particles or cells[21,22] in a microfluidic device. The so-called "inertial migration" was first observed by Segre and Silberberg, who found that the randomly discrete spherical particles in a circular pipe migrated to an annulus centered at a radial position about 0.6 times the pipe radius.[23] Theoretical analyses based on the perturbation method convincingly attribute this phenomenon to the nonlinear effect of fluid inertia.[24–27] Briefly, inertial migration is due to the balance of two types of forces. One is the shear-gradient-induced lift, F_S, arising from the curvature in the Poiseuille velocity profile that drives particles toward the wall, and the other is the wall-induced lift, F_W, produced by the wall correction with the bulk shear flow that pushes particles away from the wall.[25] An explicit lift formula is proposed to clearly embody the contribution of F_S and F_W to the inertial lift, F_L,

$$F_L = F_W + F_S = (\beta^2 G_1 + \beta\alpha G_2)\rho U_{\max}^2 a^4/H^2, \quad (1)$$

where β is the dimensionless shear rate, α is the dimensionless shear gradient, ρ is the fluid density, $U_{\max}$ is the maximum channel velocity, a is the particle diameter, H is the channel height, and G_1 and G_2 are functions of the lateral positions.[25]

Microchannels fabricated by the planar soft-lithography method commonly have rectangular cross sections. Equilibrium positions of particles in a rectangular channel are symmetrically dispersed, rather than annulus in a circular pipe.[28,29] The equilibrium positions shift closer to the wall with increasing channel Reynolds number Re ($\mathrm{Re} = \rho U_{\max} H/\eta$, where η is the dynamic viscosity) in both rectangular[30,31] and circular[32] channels. Previous studies have found that the inertial migration of randomly dispersed particles in rectangular channels can be regarded to be a two-stage process, i.e., (1) particles predominately migrate away from the channel center and the walls to a rounded rectangular ring-like region and (2) then migrate along the channel perimetric direction to finally focus at discrete equilibrium positions.[18,29,33] This process has also been observed in our recent study.[15] The first stage is similar to the inertial focusing in a pipe, both F_S and F_W driving the particles to migrate to a rounded rectangular ring-like region. After F_S and F_W cancel each other out, the rotation-induced lift F_R, whose direction is determined by the cross-product of the

a)Authors to whom correspondence should be addressed: guoqing.hu@imech.ac.cn and chenxiaodong@imech.ac.cn. Tel.: 86-10-82544298. Fax: 86-10-82543977.

angular velocity $\boldsymbol{\omega}$ and the relative particle velocity vectors $\mathbf{U_r}$, i.e., $\mathbf{F_R} \sim \boldsymbol{\omega} \times \mathbf{U_r}$, dominates the perimetric migration in the second stage.[18]

Non-spherical particles or cells commonly exist in biological and bioengineering fields, e.g., biconcave disk-like red blood cells (RBCs), cylindrical *Escherichia coli*, and ellipsoid *Euglena gracilis*. Comparing with that of spherical particles, studies on non-spherical particles are few. Inertial migrations of non-spherical particles or cells are commonly quantified by equivalent diameters, which are the diameter of spherical particles, which have same equilibrium positions with non-spherical particulates. However, the definitions of the equivalent diameters varied among different studies. Recently, several experimental investigations aiming to define the equivalent diameters are conducted.[34,35] Inertial migrations of symmetrically non-spherical particles have been found to mainly depend on their rotational diameters, D_R, i.e., their maximum size perpendicular to the rotation axis, regardless of cross-sectional shapes.[34,36]

It is natural to ask how the non-spherical particles rotate under the force exerted by ambient flow.[37–39] Two-dimensional direct simulations for inertial migration of cylindrical particles, assuming that randomly released cylindrical particles prefer to roll in a Poiseuille flow, have been previously conducted.[40,41] Recent experimental evidence has shown that there is not a dominant rotation behavior when Re is low.[34,35] Besides, remarkable focusing of non-spherical particles rarely occurs.[36] Above a critical Re (about 50), non-spherical particles predominantly adopt to preferred rotational axes and migrate to remarkable equilibrium positions.[34,35,42] For instance, cylindrical and ellipsoid particles prefer to tumble while disk-like particles prefer to roll. Because of the anisotropy of non-spherical particles, the shape effect may continuously change the angular velocity and sweeping area of particles, leading to periodically varying lift force and equilibrium position. For example, the tumbling motion of ellipsoid particles has been found to predominantly change the wall-induce lift and thus periodically shift the particle toward and away from the wall.[35,43]

Rotational diameter has been used to roughly determine equilibrium position. However, the detailed migration process and the influence of Re to the equivalent diameter for equilibrium position are yet to be explored. In this paper, we study numerically the migration dynamics and equilibrium positions of cylindrical particles in rectangular microchannels. Detailed particle motions and dynamical distributions of surface stress are addressed. Distributions of lateral forces at cross sections with different aspect ratios are obtained systematically. Comparisons of equilibrium positions with spherical particles with different diameters are conducted. In addition, equilibrium positions of cylindrical particles with different aspect ratios and blockage ratios are carried out. Finally, an inertial migration of a special cylindrical particle, disk-like particle, is also explored.

II. METHOD

A. Computational methods

As shown in Fig. 1(a), we consider a neutrally buoyant rigid cylindrical particle, with axis length L and diameter D, suspending in a Poiseuille flow within a straight rectangular microchannel. The origin of coordinate is located at the center of the channel inlet. The x-, y-, and z-coordinates represent the

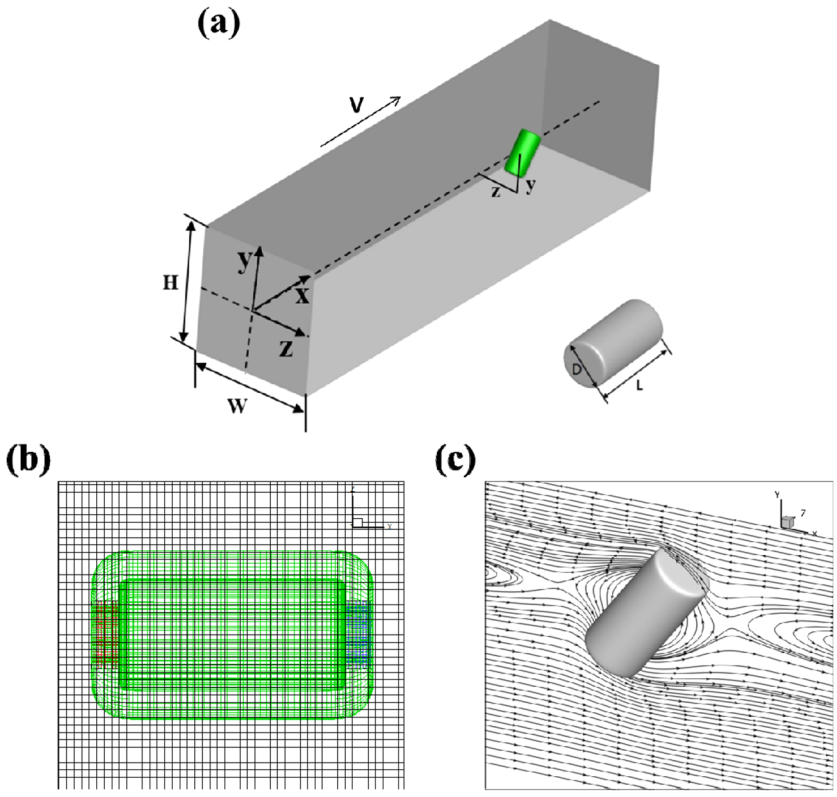

FIG. 1. (a) Schematic illustration of a cylindrical particle suspending in a pressure-driven flow within a rectangular microchannel. (b) The computational domain consists of four component grids, i.e., the channel Cartesian grids (black lines), the body fitted grids for the particle with two poles removed (green lines), and the grids for two poles (red and blue lines). (c) Typical streamlines around a cylindrical particle for the flow field with the relative velocity based on the center of the cylindrical particle.

directions of the mainstream, height, and width of the cross section, respectively. The general function of the lift force (F_L) can be written as a function of the geometrical and physical parameters[15,44]

$$F_L = F\left(D, L, y, z, t, H, W, U_{\max}, \eta, \rho\right), \tag{2}$$

where (y, z) is the lateral coordinate in the y-z plane, t is the time, and W is the width of the channel. Among these ten parameters, H, $U_{\max}$, and ρ are used to nondimensionalize the system. According to the Buckingham π theorem,[45] the general formula of lift force thus depends on seven nondimensional quantities,

$$\begin{aligned} F_L &= F\left(\frac{L}{H}/\frac{D}{H}, \frac{L}{H}, \frac{y}{H}, \frac{z}{H}, 1, \frac{W}{H}, 1, \frac{\eta}{\rho U_{\max} H}, 1, \frac{t}{H/U_{\max}}\right) \\ &= F\left(\frac{L}{D}, \kappa, \frac{2y}{H}, \frac{2z}{H}, \frac{W}{H}, \mathrm{Re}, t\cdot\gamma\right). \end{aligned} \tag{3}$$

The aspect ratio of cylindrical particles, L/D, characterizes the particle nonsphericity. The blockage ratio, $\kappa = L/H$, determines the main size of the particle in comparison to the channel height. L/D and κ jointly determine the disturbance on the basic flow due to the presence of the cylindrical particle. The time is calculated by $t\cdot\gamma$, where $\gamma = 2U_{\max}/H$ is the average shear rate. The lateral position of the particle center is ($2y/H$, $2z/H$), where both $2y/H$ and $2z/H$ vary from 0 to 1, indicating the position from the channel center to the walls. W/H determines the velocity profile along the long axis of cross section varying from parabolic to plug-shaped with W/H deviating from unity. Re reflects the intensity of inertial nonlinearity of the undisturbed flow. Similar to that for spherical particles,[25] we adopt the dimensionless lift coefficient, C_L, to measure the inertial force acting on cylindrical particles,

$$C_L = \frac{F_L}{\left(\rho U_{\max}^2 {D_N}^4/H^2\right)}, \tag{4}$$

where the nominal diameter, D_N, is the diameter of a spherical particle with identical volume with the cylindrical particle. Our simulations investigate the cases that cylindrical particles migrate in microchannels with a fixed H of 50 μm. The medium surrounding the particles is water.

Incompressible Navier-Stokes (N-S) equations for fluid flow coupled with Newton's second law of motion for particles are numerically solved on structured overlapping grids with the Overture object-oriented framework.[46] The N-S equations are

$$\nabla\cdot\mathbf{u} = 0, \tag{5}$$

$$\frac{\partial\mathbf{u}}{\partial t} + (\mathbf{u}\cdot\nabla)\mathbf{u} = -\frac{1}{\rho}\nabla p + \frac{\eta}{\rho}\nabla^2\mathbf{u}, \tag{6}$$

where $\mathbf{u}$ is the fluid velocity tensor and p is the pressure. The gravitational force is neglected here as the density of particles is equals to that of the fluid. The force acting on the cylindrical particle is obtained by integrating the surface stress over the particle surface. The torque is obtained by integrating the cross product of distance to the particle center and the surface stress over the particle surface. The equations for particle motions are thus

$$m_p\frac{d\mathbf{U}_p}{dt} = \int_\Sigma(-p\mathbf{1}+\boldsymbol{\tau})\cdot\mathbf{n}d\sigma, \tag{7}$$

$$\frac{d\left[\mathbf{A}(t)\boldsymbol{\omega}_p\right]}{dt} = \int_\Sigma(\mathbf{x}-\mathbf{x}_{cm})\times[(-p\mathbf{1}+\boldsymbol{\tau})\cdot\mathbf{n}]d\sigma, \tag{8}$$

where $\boldsymbol{\omega}_p = [\omega_1\ \omega_2\ \omega_3]^T$ is the angular velocity vector, $\mathbf{1}$ is the unit tensor, $\boldsymbol{\tau}$ is the shear rate tensor, $\mathbf{n}$ is the unit normal vector of particle surface, $\mathbf{A}$(t) is the moment of inertia tensor of the particle, and $\mathbf{x}_{\mathrm{cm}}$ is the position of the mass center of the particle. We introduce the principle axes of inertia $\mathbf{e}_i$ and corresponding moment of inertia I_i into our system. $\mathbf{A}$(t) is a symmetric positive definite tensor,

$$\mathbf{A} = \mathbf{E}\boldsymbol{\Lambda}\mathbf{E}^T, \tag{8a}$$

where $\Lambda = \mathrm{diag}(I_1, I_2, I_3)$, $\mathbf{E} = [\mathbf{e}_1\ \mathbf{e}_2\ \mathbf{e}_3]$, $\mathbf{e}_i\cdot\mathbf{e}_j = \delta_{ij}$, $\mathbf{E} = \mathbf{E}^{-1}$. Note that $\boldsymbol{\Lambda}$ is independent with time. Since the axes of inertia rotate with the cylindrical particle, the derivative versus time is

$$\dot{\mathbf{E}} = \boldsymbol{\Omega}\mathbf{E}, \tag{8b}$$

where

$$\boldsymbol{\Omega} = \begin{bmatrix} 0 & -\omega_3 & \omega_2 \\ \omega_3 & 0 & -\omega_1 \\ -\omega_2 & \omega_1 & 0 \end{bmatrix}, \tag{8c}$$

and Eq. (8) can be rewritten as

$$\boldsymbol{\Omega}\boldsymbol{A}\boldsymbol{\omega}_p + \mathbf{A}\dot{\boldsymbol{\omega}}_p = \int_\Sigma(\mathbf{x}-\mathbf{x}_{cm})\times[(-p\mathbf{1}+\boldsymbol{\tau})\cdot\mathbf{n}]d\sigma. \tag{8d}$$

The overlapping grid method is applied to the computational domain by means of the Overture object-oriented framework. To obtain good computational efficiency and precision, the computational domain is constructed by four overlapping subzones with independent structured grids [Fig. 1(b)], i.e., the Cartesian grids for the channel, the body-fitted grids for the cylindrical particle with two poles removed, and the body-fitted grids for two poles. Such arrangement of grids avoids the singularity at two poles. The information exchanges of the subzones are achieved via interpolation between every two overlapped blocks, while the grid updates every time step to guarantee the quality. The overlapping grid method is robust in dealing with fluid flow around a moving solid boundary. The interaction between particle surface and surrounding flow can thus be predicted with high precision. For example, Fig. 1(c) shows that smooth streamlines around the cylindrical particle can be obtained at every time step.

The no-slip boundary conditions are implemented on the channel walls and the particle surface. The velocity profile for the Poiseuille flow in a rectangular cross section is imposed on the inlet,[47]

$$\begin{aligned} u(y,z) = \frac{4H^2\Delta p}{\pi^3\eta L_C}\sum_{n,odd}^{\infty}\frac{1}{n^3}\left[1-\frac{\cosh\left(n\pi\frac{z}{H}\right)}{\cosh\left(n\pi\frac{W}{2H}\right)}\right] \\ \times\sin\left[n\pi\left(\frac{y}{H}+\frac{1}{2}\right)\right], \end{aligned} \tag{9}$$

where Δp is the pressure difference between the inlet and the outlet and L_C is the channel length. The constraint of $p + \partial p/\partial n = 0$ is imposed as an outflow boundary condition.

In the time stepping, viscous term is implicitly treated with an implicit factor of 0.5 (the Crank-Nicolson method) and the other terms are explicitly treated with a second-order Adams predictor corrector.[48] A second-order centered difference scheme is applied to the spatial discretization of the convective term and viscous term.[48] A stabilized bi-conjugate gradient (BiCG-Stab) method with the incomplete preconditioner (LU) is applied to iteratively solve the linear equations derived from the pressure equation. The Courant-Friedrichs-Lewy (CFL) number is set to be 0.75 to guarantee the stability of the simulations. The solving process is done by the PETSc software package,[49] which has an interface to the Overture framework.

B. Measurement of lift force

To obtain the lift force experienced by a cylindrical particle at certain lateral position, $(2y/H, 2z/H)$, a constraint is adopted to fix the cross-sectional position by setting lateral velocity (U_y and U_z) to be constant zero, while the particle moves freely in the axial direction of the channel. Under this constraint, the cylindrical particle is initially placed at a predefined lateral position and then driven by the force imposed by the surrounding flow to translate and rotate. When the translational and rotational motions both reach steady states, the C_L component (C_{Ly} and C_{Lz}) can be obtained by integrating the hydrodynamic forces acting on the particle. This constraint method has been previously utilized by our group[15,50,51] and other groups[22,33] to obtain the inertial lift force acting on spherical particles and deformable droplets. Due to the tumbling motion of cylindrical particles, the inertial lift is a constant with small periodical oscillations in the present study. We here average the lift force coefficient for several oscillation periods at steady state to obtain the averaged lift force coefficient C_{av}. By varying the lateral position and carrying out the corresponding simulation, the spatial distribution of C_{av} in the cross section can be obtained as well as the tendency of inertial migration toward equilibrium positions.

C. Grid independence study

A grid independence study is conducted with three grid resolutions. The grid resolution is measured by the ratio of the size of the background grid, Δx, to L, varying from 0.1 to 0.05. Figure 2(a) shows variations of F_L acting on the cylindrical particle constrained at (0.5, 0) for three $\Delta x/L$ under Re = 100. The differences among the results of the two finer grid resolutions are small. Figure 2(b) shows the variation of C_{av} along the y-axis. Negligible differences are also observed. Further comparisons for C_{av} under Re = 30 and 300 are shown in Figs. 2(c) and 2(d). Therefore, the grid resolution of $\Delta x/L = 0.075$ is used in subsequent simulations due to the adequate accuracy and proper numerical cost. The channel length varies from $15H$ to $80H$, which is enough for a cylindrical particle to reach the steady state. The maximum grid number is about 25 000 000. Totally over 700 simulations are carried out to produce a systematical investigation on the inertial migration of cylindrical particles.

D. Methods' validation

The equilibrium position at cross section can be obtained by the constraint method when $C_{av} = 0$. We find that equilibrium positions by the constraint method are almost identical to the free model in which particles move without constraint. The solid line in Fig. 3(a) shows the trajectory of the center of a free cylindrical particle released from initial lateral position of (0.4, 0). After reaching the steady state, the rotating particle oscillates periodically around a time-averaged equilibrium position. The time-averaged equilibrium position is at (0.534, 0) as represented with a black dashed line in Fig. 3(a). The magnitude of the periodical oscillations Δ is only 1.25% of the L. The red dashed line in Fig. 3(a) represents the equilibrium position obtained by the constraint method, (0.536, 0). The negligible difference between the two equilibrium positions indicates that the constraint method is able to obtain the equilibrium position. Figure 3(b) further confirms the

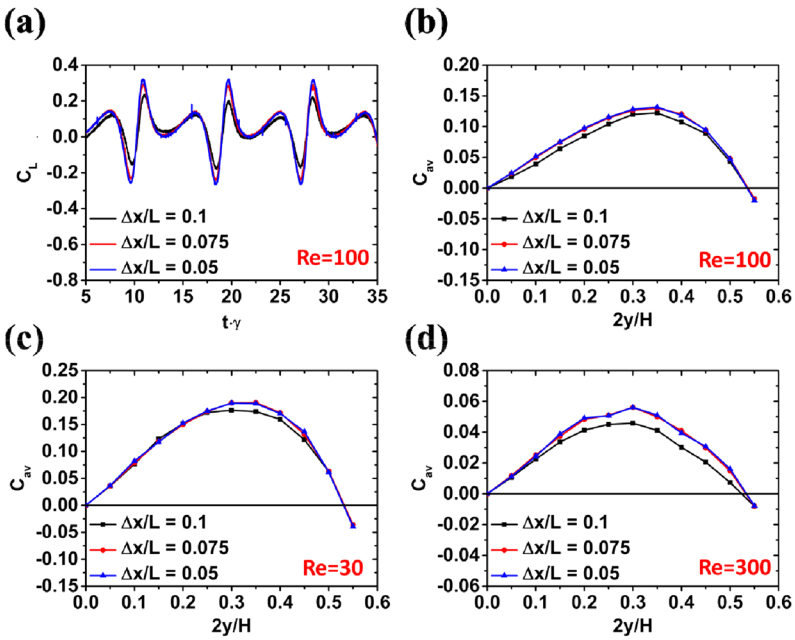

FIG. 2. Comparisons of lift forces under three grid resolutions for cylindrical particles with $L/D = 2$ and $\kappa = 0.3$ in a rectangular channel with $W/H = 1$. (a) C_L at Re = 100; (b) C_{av} at Re = 100, (c) C_{av} at Re = 30; (d) C_{av} at Re = 300.

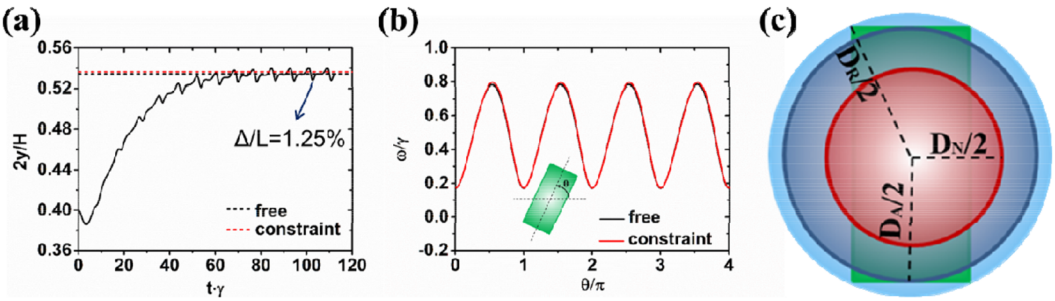

FIG. 3. Comparisons of cylindrical particles with and without constraint at Re = 100 for cylindrical particles with $L/D = 2$ and $\kappa = 0.3$ in a rectangular channel with $W/H = 1$: (a) Equivalent equilibrium position. (b) Angular velocity. (c) D_N, D_A, and D_R corresponding to spherical particles with the equivalent volume diameter, axial length, and rotational diameter of the cylindrical particle as diameter, respectively.

excellent agreement in the angular velocity for the particles with and without constraint.

The small oscillation magnitude of the equilibrium position, $\Delta/L = 1.25\%$, suggests that cylindrical particles have well-defined equilibrium positions that can be equivalent to those of spherical particles. Figure 3(c) shows three types of diameters, i.e., nominal diameter D_N, rotational diameters D_R, and axial length diameter D_A. The axial length diameter D_A is equal to the axial length of the cylindrical particle. Inertial forces and equilibrium positions of spherical particles with three types of diameters will be calculated and compared with those of cylindrical particles in Sec. III.

III. RESULTS AND DISCUSSION

A. Particle motion and surface stress

For a typical case, Fig. 4(a) show the variation of C_L in the y and z directions, C_{Ly} and C_{Lz}, as well as orientations of the particle looking in directions perpendicular to the x-y plane (first row) and x-z plane (second row). The mass center of the cylindrical particle is constrained at (0.5, 0.3). From both view directions, the particle tumbles counterclockwise. C_{Ly} and C_{Lz} vary in-phase, while the amplitude of C_{Ly} is larger than that of C_{Lz} due to which the particle is closer to the wall in the y direction. Variations of C_{Ly} and C_{Lz} are smooth when the long axis of cylindrical particles is near the orientation in-line with the flow, while sharp variations are observed when the long axis deviates from the orientation.

To discuss variations of lift force and torque acting on the cylindrical particle in detail, we simulate a situation when the particle is constrained at (0.5, 0), where the particle only rotates counterclockwise in the z direction. Figure 4(b) shows the variation of C_L with θ, as well as the minimum distance between the particle surface and the wall, Δy, nondimensionalized by $H/2$. Figure 4(c) shows the variation of the dimensionless torque, C_{tor}, as well as the angular velocity, ω, nondimensionalized by γ. The C_{tor} is defined as $C_{tor} = T_{tor}/(\rho U_{\max}^2 D_N^5/2H^2)$, where T_{tor} is the torque. All the variables change periodically over each integer of θ/π, which corresponds to half the rotation

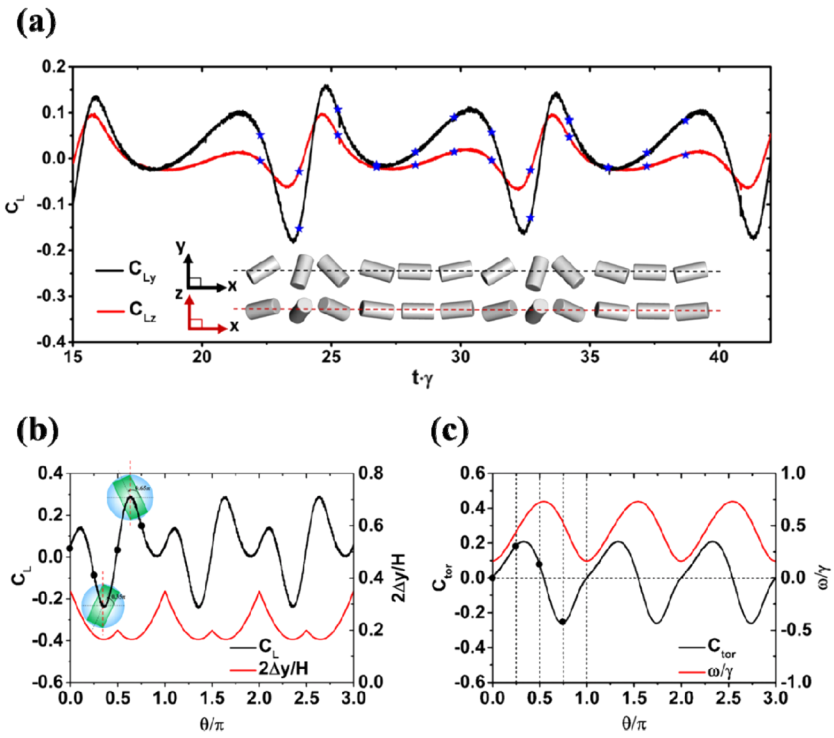

FIG. 4. (a) C_L components for a cylindrical particle located at (0.5, 0.3) with orientations of the particle looking in directions perpendicular to the x-y plane (first row with the black dashed line) and the x-z plane (second row with the red dashed line). Variations of C_L and $2\Delta y/H$ (b), C_{tor} and ω/γ (c) for a cylindrical particle located at (0.5, 0). The dots are marked where $\theta = 0$, $\pi/4$, $\pi/2$, and $3\pi/4$. The results are for cylindrical particles with $L/D = 2$ and $\kappa = 0.3$ in a rectangular channel with $W/H = 1$ at Re = 100.

cycle of the particle. Two peaks and two troughs of C_L exist within one θ/π, as shown in Fig. 4(b). Initially, C_L increases when θ/π varies from 0 to about 0.10 and the particle is pushed toward the channel wall. The value of C_L then reduces sharply as the particle tilts, indicating that the lift force tends to push the particle back toward the channel center. The minimum C_L is obtained when the diagonal line of the particle cross section in the y-x plane is nearly perpendicular to the wall at $\theta/\pi \approx 0.35$. After that, C_L increases rapidly and obtains a maximum value at $\theta/\pi \approx 0.65$ when the other diagonal line is nearly perpendicular to the wall. Those two orientations also correspond to the situations when $2\Delta y/H$ has the minimum value as shown in Fig. 4(b). Figure 4(c) shows that ω/γ has its maximum value at $\theta/\pi \approx 0.50$, i.e., the cylindrical particle has a larger angular velocity when diagonal lines rotate to and away from the direction perpendicular to the wall. Large disturbances are thus imposed on the lift force because of the angular momentum. When diagonal lines are nearly perpendicular to the wall, extreme values of the lift are observed as the disturbances in the direction of lift force reach their peaks. As shown in Fig. 4(c), C_{tor} is near zero at $\theta/\pi = 0$, where the angular velocity reaches its minimum value. As the particle rotates, C_{tor} increases to its peak near $\theta/\pi \approx 0.35$ and decreases to zero, when ω/γ is at its largest. C_{tor} continues to decrease to its smallest and subsequently increases back to near zero at $\theta/\pi = 1$.

The magnitudes and directions of the lift and torque can be determined by the distribution of surface stresses acting on the particle surface. The dimensionless surface stress is defined as $C_f = f/(0.5\rho U_{\max}^2\ \kappa^2)$, where $f = (-p\mathbf{1} + \boldsymbol{\tau})\cdot\mathbf{n}$ is the surface stress. Figure 5 shows the distribution of surface stresses for four rotation angles marked with dots in Fig. 4, i.e., $\theta = 0$, $\pi/4$, $\pi/2$, and $3\pi/4$. The magnitudes of C_f are represented with surface contours, while the directions of the surface stresses are represented with vectors. Figure 5(a) shows a smooth distribution of surface stresses acting on the cylindrical particle as $\theta = 0$. Figures 5(b)–5(d) show that large surface stresses emerge at the end near the channel wall when the particle's long axis

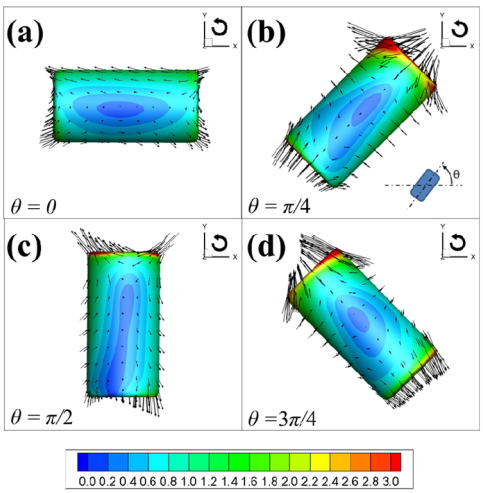

FIG. 5. The distribution of the surface stress coefficient C_f with the change of θ. The vectors donate the orientation of the stress and the contours donate the magnitude. (a) $\theta = 0$, (b) $\theta = \pi/4$, (c) $\theta = \pi/2$, and (d) $\theta = 3\pi/4$.

is not in line with the channel axis. As the lift is negative at $\theta = \pi/4$ but positive at $\theta = \pi/2$ and $3\pi/4$ [Fig. 4(a)], the surface stresses acting on the end near the wall mainly direct away from the wall at $\theta = \pi/4$ [Fig. 5(b)] while they direct toward the wall as $\theta = \pi/2$ [Fig. 5(c)] and $3\pi/4$ [Fig. 5(d)]. The magnitudes of surface stresses for $\theta = \pi/2$ are obviously smaller than those for $\theta = \pi/4$ and $3\pi/4$. As the torque is positive at $\theta = \pi/4$ and $\pi/2$ but negative at $\theta = 3\pi/4$ [Fig. 4(c)], the surface stresses on the end near the wall tend to drive the cylindrical particle to rotate clockwise at $\theta = \pi/4$ and $\pi/2$, while counterclockwise at $\theta = 3\pi/4$. By contrast, surface stresses acting on the end away from the wall tend to drive the cylindrical particle to rotate with counterclockwise at $\theta = \pi/4$ and $\pi/2$, while clockwise at $\theta = 3\pi/4$. The main direction of surface stresses is also opposite to the direction of lift force on the cylindrical particle. However, the magnitudes of surface stresses acting on the end away from the wall are smaller than that acting on the end near the wall. Therefore, we conclude that the surface stresses acting on the end near the wall are the major contributors to the particle rotation.

B. Force distributions and particle migration

A series of direct numerical simulations are conducted to investigate the migration behavior of cylindrical particles at different Re. We here investigate the cylindrical particle with $L/D = 2$ and $\kappa = 0.3$ in a microchannel with two different aspect ratios, i.e., $W/H = 1$ and 2. The total number of the cases for the two W/H is 175 and 440, respectively. We regard the cross-sectional positions, where the average lift force is zero, as equilibrium positions. An equilibrium position is stable if the particle will be pushed back once it is disturbed away from the position. An unstable equilibrium position is an equilibrium position that a small disturbance will drive the particles away from the initial position.

Figure 6 shows the distributions of lift vectors in the cross sections along with particle trajectories under Re varying from 50 to 200. Figures 6(a)–6(c) demonstrate that there are always four stable equilibrium positions for a square channel ($W/H = 1$). As shown in Figs. 6(d) and 6(e), only two stable equilibrium positions appear at the long wall centers with $W/H = 2$ for Re varying from 50 to 100, while two other equilibrium positions at the short wall centers are unstable. Many groups have reported two equilibrium positions of spherical particles centered at the two long walls if the W/H highly deviates from unity.[22,35] However, six or even eight equilibrium positions have also been observed in microchannels with similar W/H.[52] Figure 6(e) shows that the unstable equilibrium positions of cylindrical particles turn to stable as Re increases to 200.

We have previously observed the so-called two-stage process during the inertial migration of spherical particles in rectangular channels with $W/H = 2$.[15] By tracking the particle trajectories according to lift vectors, the two-stage process is also found for cylindrical particles as shown in Figs. 6(a)–6(f), i.e., in the first stage, particles predominately migrate away from the channel center and the walls to form a rectangular ring, and, in the second stage, particles migrate along the channel perimetric direction and finally focus at discrete equilibrium positions. In the first stage, both F_S

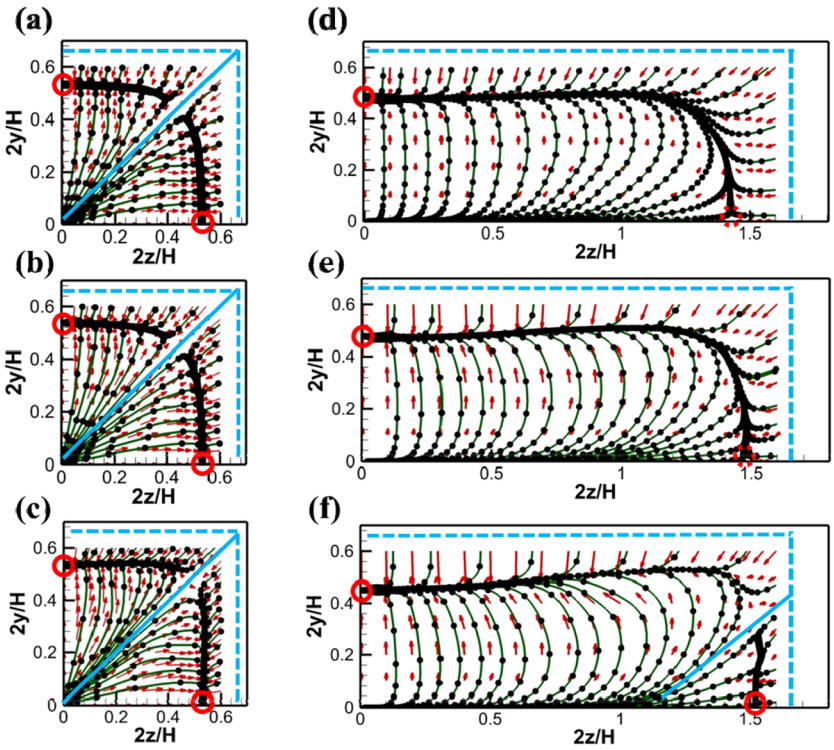

FIG. 6. Distributions of lift force acting on a cylindrical particle in a quarter cross section of the square channel with $W/H = 1$ [(a)-(c)] and the rectangular channel $W/H = 2$ [(d)-(f)] under Re = 50 [(a) and (d)], 100 [(b) and (e)], 200 [(c) and (f)]. Each red vector represents the lift force experienced by a cylindrical particle with its center at the origin of the vector. The trajectories of the cylindrical particle center are represented with the green lines. The small black full circles are put on the trajectories with same nondimensional time units. The solid-line red circles represent stable equilibrium positions and the dashed-line ones represent unstable equilibrium positions. The blue dashed lines confine the area that the center of the particle can reach. The blue solid lines are the separatrices dividing the cross sections into two portion, in each of which particles will focus to the corresponding equilibrium position.

and F_W drive the particles to migrate to a rounded rectangular ring-like region where two forces cancel each other out. The rotation-induced lift F_R then becomes the dominator in the second stage and drives the cylindrical particles with smaller migration velocity since F_R is much weaker than F_S and F_W.[18,24,53]

We further investigate the cases under Re = 300 and 400 as shown in Fig. 7. With the increase of Re, the larger F_R will act on cylindrical particles and thus induces a velocity component directing particles to equilibrium positions before a remarkable rectangular ring of particles is formed. The rectangular ring becomes less remarkable in the square channel with $W/H = 1$ [Figs. 7(a) and 7(b)], which can also be observed near the short wall in the rectangular channel with $W/H = 2$ [Fig. 7(d)]. The blue solid lines in Fig. 7 divide the cross sections into two portions, in each of which particles will focus to the corresponding equilibrium position. In the rectangular channel with $W/H = 2$, Figs. 7(c) and 7(d) show a more obvious migration toward equilibrium positions at the short wall centers, with the increasing Re due to the larger portion.

C. Comparisons with spherical particles

It is a natural question that how the forces experienced by cylindrical particles compares to that of spherical particles. There are three types of diameters as shown in Fig. 3(c), i.e., nominal diameter, D_N, axial length diameter, D_A, and rotational diameter, D_R. Figures 8(a)–8(d) show the comparison of C_{av} for cylindrical particles and spherical particles with D_N, D_A, and D_R as diameters when Re deviates from 50 to 200 with an interval of 50. For the cylindrical particle and the spherical particle with a diameter of D_N, the curves of C_{av} are

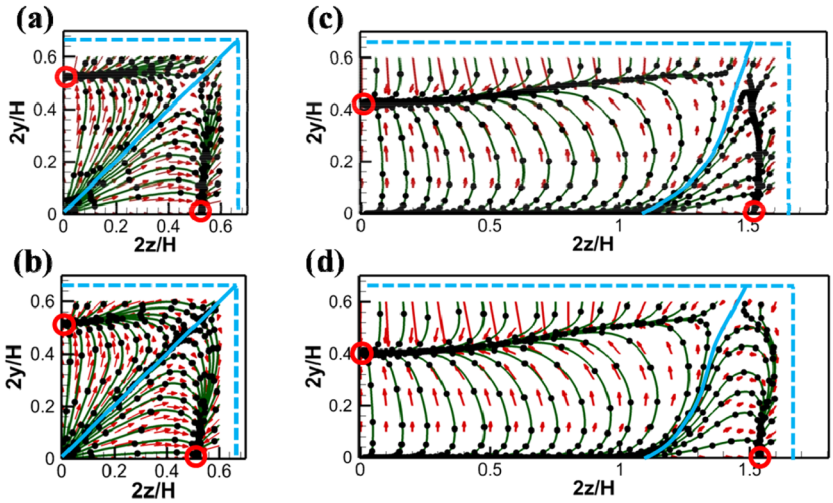

FIG. 7. Distributions of lift force acting on a cylindrical particle in a quarter cross section of the square channel with $W/H = 1$ [(a) and (b)] and the rectangular channel with $W/H = 2$ [(c) and (d)] under Re = 300 [(a) and (c)], 400 [(b) and (d)].

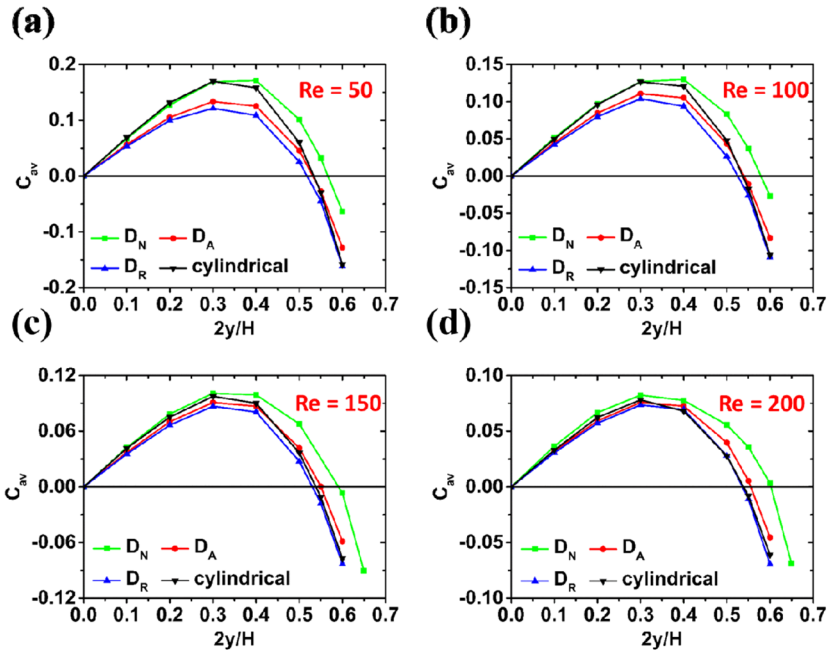

FIG. 8. Comparison of C_{av} at Re = 50 (a), 100 (b), 150 (c), and 200 (d) in channels with $W/H = 1$. Here D_N, D_A and D_R are defined in Fig. 3(c).

close to each other near the channel center for all Re. Meanwhile, the difference between the two curves of C_{av} increases as particles are close to the wall. Near the wall, the curves for the cylindrical particle and the spherical particle with diameter of D_R almost overlap. Near the equilibrium position, the curve for cylindrical particles is close to that for the spherical particle with a diameter of D_A at Re = 50. As Re increases, the curve for cylindrical particles shifts to be close to that for the spherical particles with a diameter of D_R. The curves for the cylindrical particle and the spherical particle with a diameter of D_R almost overlap at Re = 200.

It is of practical interest to characterize equilibrium positions of cylindrical particles by single diameters. We thus define the equivalent diameter of a cylindrical particle to be the diameter of the corresponding spherical particle that has the same equilibrium position. Figure 9(a) shows the variations of the equilibrium positions obtained from Figs. 8(a)–8(d) for $W/H = 1$. One can use D_A as the equivalent diameter when Re = 50, while the proper equivalent diameter can be D_R when Re = 200 [Fig. 9(a)]. As in previous studies,[27,30,31] we find that spherical particles migrate to the wall as Re increases from 50 to 200. The variation of equilibrium position with Re for cylindrical particles is also found to be smaller than that for the spherical particles [Fig. 9(a)]. The variation of equilibrium position is only 0.83% of the L when Re varies from 50 to 200. This small variation may be due to that the increase of Re is balanced out by the non-spherical shape of the cylindrical particle. The increase of the equivalent diameters (from D_A to D_R) gives rise to the increase of wall-induced force. The increase of shear-induced force with Re is thus balanced out by the wall-induced force.

We also carry out a series of simulations to obtain the equilibrium position for cylindrical particles at the long wall center for a channel with $W/H = 2$. Figure 9(a) has shown that equilibrium position of the spherical particle with D_A is far away from that for the cylindrical particle. Therefore, Fig. 9(b) compares the variation of the equilibrium position for cylindrical particles with spherical particles with diameters of D_A and D_R as Re varies from 50 to 200. As shown in Fig. 9(a), the equilibrium position of the cylindrical particle is far away from that of the spherical particle with D_N [Fig. 9(b)]. D_A can be used as the equivalent diameter when Re = 50. The equivalent

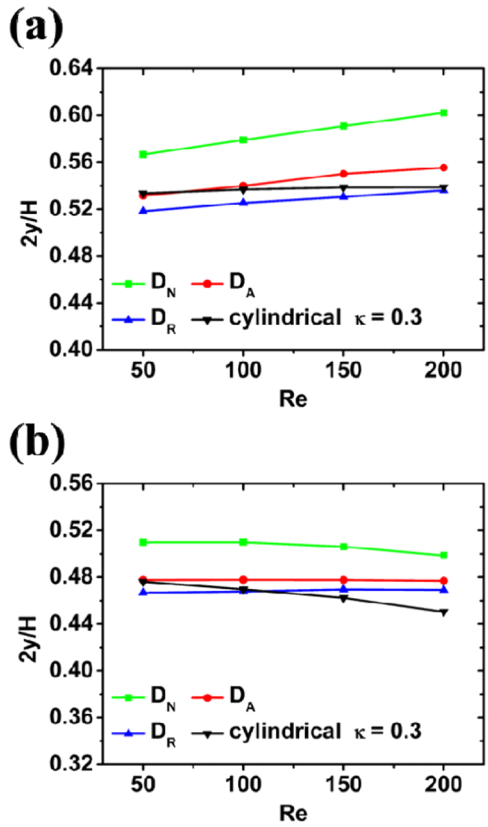

FIG. 9. Comparison of the variation of stable equilibrium positions at different Re in a channel with $W/H = 1$ (a) and $W/H = 2$ (b).

diameter changes to D_R when Re = 100. Further increase of Re gives rise to an equivalent diameter larger than D_R. Intuitively, the increasing Re causes the increase of the influence of cylindrical particles on surrounding flow, leading to the increase of the equivalent diameter. The wall-induced force thus increases against the shear-induced force to push the cylindrical particle further away from the wall.

D. The influence of κ and L/D

The blockage ratio, $\kappa = L/H$, determines the main size of the particle in comparison to the channel height. A series of simulations are carried out for $\kappa = 0.2$ and 0.15 to study the influence of κ to the equilibrium position with $W/H = 1$. Figures 10(a) and 10(b) show that variations of the equilibrium position with Re for $\kappa = 0.2$ and 0.15 are similar to the results of the cylindrical particle with $\kappa = 0.3$ in Fig. 9(a), i.e., the equivalent diameter varies from D_A to D_R with the increasing Re. Besides, the equilibrium position is further away from the wall than that of the spherical particle with a diameter of D_R as at Re = 200. Figure 10(c) compares the equilibrium positions of cylindrical particles with $\kappa = 0.15$, 0.2, and 0.3 under different Re. The equilibrium positions obviously shift away from the wall with increasing κ. Although the changes of equilibrium positions are all very small under different Re, the shift to the wall with increasing Re is observed. Besides, the shift distance due to the change of Re increases with the increasing κ. Figure 10(d) shows the variation of angular velocities with the rotation angle of cylindrical particles (with $\kappa = 0.15$, 0.2, and 0.3) located at (0.5, 0) under Re = 100. The angular velocities of cylindrical particles are almost independent with κ, similar to that for ellipsoidal particles.[54]

The above discussion is about cylindrical particles with $L/D = 2$. The effect of L/D is yet to be explored. We thus vary D and fix L to study the inertial migration of cylindrical particles with $L/D = 3$ and 4. Figure 11(a) shows that equilibrium positions slowly shift to the wall with increasing L/D. The slow variations with Re are also observed, while the equilibrium position of cylindrical particles with $L/D = 3$ and 4 begins to shift away from the wall when Re varies from 150 to 200. Figure 11(b) shows C_L curves for cylindrical particles with different L/D located at (0.5, 0). The magnitude of oscillation increases with L/D, while the rotation angles have extreme C_L values increasing with L/D. Figure 11(c) shows that the variations of angular velocities for different L/D are almost in-phase. Meanwhile, the oscillation amplitude increases with L/D. Jeffery has demonstrated that an isolated oblate ellipsoid in an unbounded linear shear flow undergoes a periodic tumbling motion around the vortex axis.[54] The period of the oblate ellipsoid, T_{ell}, depends on its shape,

$$T_{ell} = \frac{2\pi}{\gamma_0}\left(AR + \frac{1}{AR}\right), \tag{10}$$

where γ_0 is the shear rate at the particle center in an undisturbed flow and AR is the aspect ratio of the ellipsoid. Analogously, we normalize the period of cylindrical particles, T, with $2\pi(L/D + D/L)/\gamma_0$ as shown in Fig. 11(d). The normalized period is found to decrease with increasing L/D. Additionally, there is a proportional relationship between Re and the normalized period. With the increasing Re, the influence of edges on the two ends of the cylindrical particle is strengthened, indicating a smaller L/D. Therefore, the variations of a normalized period with increasing Re and L/D show an opposite trend.

E. A special case: Disk-like particle

We have studied inertial migration of cylindrical particles with $L/D > 1$. When $L/D < 1$, the cylindrical particle becomes a disk-like particle. Here, we consider two types of disk-like particles with $L/D = 4{:}15$ and different edge shapes. One has sharp edges with a radius of $L/16$ and the other has smooth edges with a radius of $L/2$. The blockage ratio of disk-like particles is defined as $\kappa_d = D/H$. Different from cylindrical particles with $L/D > 1$, we find that disk-like particles tend to

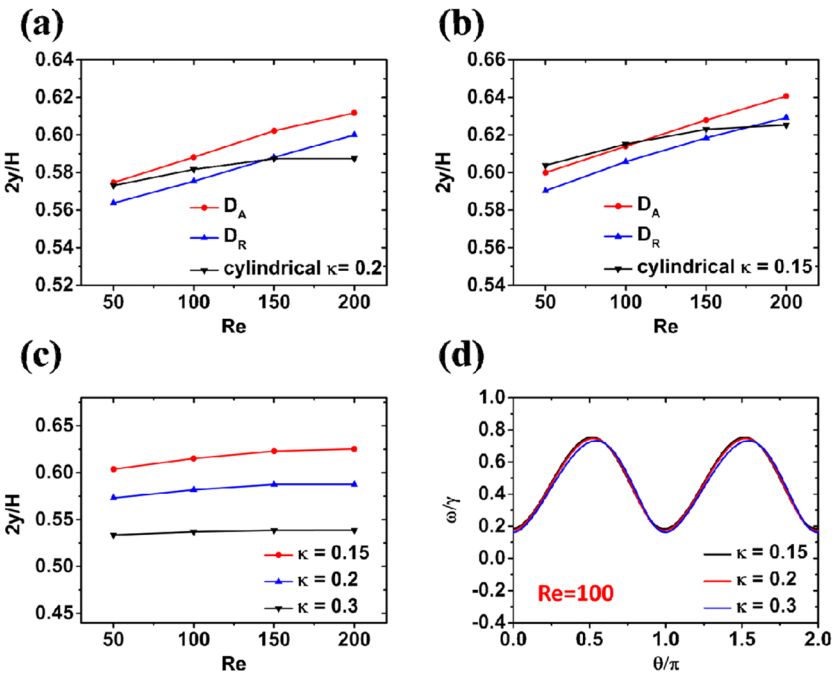

FIG. 10. The influence of κ for cylindrical particles in a channel with $W/H = 1$. Comparison of equilibrium positions with spherical particles for cylindrical particles: (a) $\kappa = 0.15$ and (b) $\kappa = 0.2$. Comparing equilibrium positions (c) and ω/γ (d) of cylindrical particles with $\kappa = 0.15$, 0.2, and 0.3.

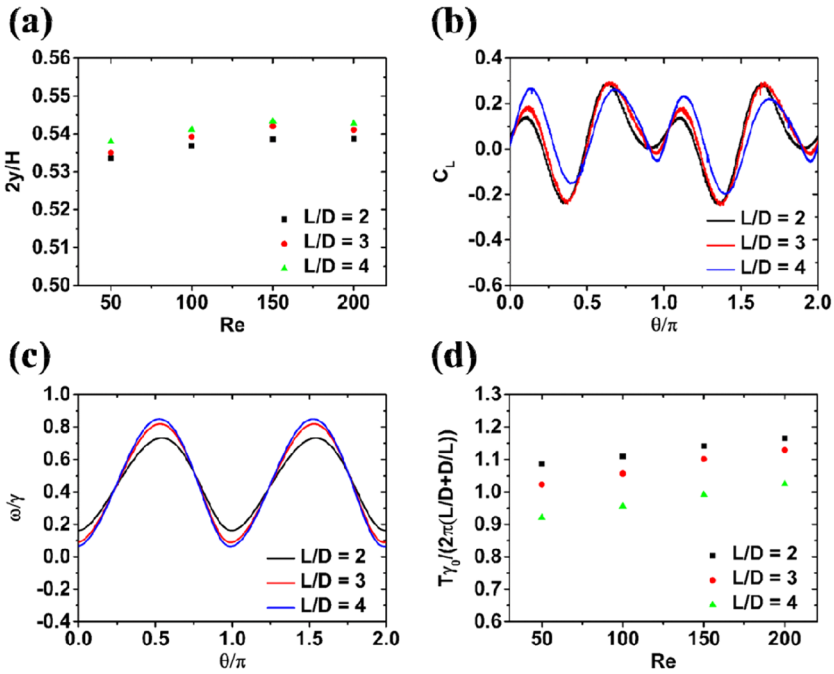

FIG. 11. The influence of aspect ratio (L/D = 2, 3 and 4) for cylindrical particles in a channel with W/H = 1: (a) equilibrium positions, (b) lift force, (c) angular velocity, and (d) normalized period. (b)–(d) are for a cylindrical particle located at (0.5, 0).

roll for Re varying from 50 to 200 [the corresponding particle Reynolds number in our paper $\mathrm{Re}_p = 2\rho U_{\max} D^2/(H\eta) = 2$–30]. This founding agrees with the previous observations that a disk-like particle with L/D = 1:2 prefers to roll in a shear flow when Re_p is less than 230.[55]

Figure 12 compares the variation of equilibrium positions with Re for disk-like particles with $\kappa_d = 0.3$ and a spherical particle with a diameter of D_R, which is equal to D. Equilibrium positions of disk-like particles are closer to the channel center than those of the spherical particle with a diameter of D_R. The distinctions increase with the increase of Re indicating slower variations of equilibrium positions of disk-like particles. Meanwhile, equilibrium positions of sharp-edged particles are closer to the channel center than those of smooth-edged particles.

It has been known that a biconcave disk-like RBC shows two basic motions in shear flows, i.e., tumbling motion under low shear stress and rolling motion under higher shear stress.[56,57] Di Carlo *et al.* have experimentally studied the inertial migration of RBCs in rectangular microchannels[42] and found that RBCs behave as rigid particles under Re = 60. RBCs migrate to four equilibrium positions near the wall center and then roll with the short axis parallel to the wall. Available experimental evidence later reveals that the RBC under rolling motion has a stabilized cell membrane and can maintain its biconcave disk-like shape.[58–60] Under physiological conditions, a mature RBC is about 6–8 μm in diameter and 2 μm in thickness. A smooth-edged disk-like particle with L/D = 4:15 is used to model the RBC with 7.5 μm in diameter and 2 μm in thickness. Fixing the particle size, we investigate the influence of the blockage ratio. The distinctions between equilibrium positions of the RBC-like particles and the corresponding spherical particles with a diameter of D_R become larger with the increasing κ_d and Re [Figs. 13(a)–13(c)]. As shown in Fig. 13(d), the angular velocity decreases with the increasing Re, with smoother variation for smaller κ_d.

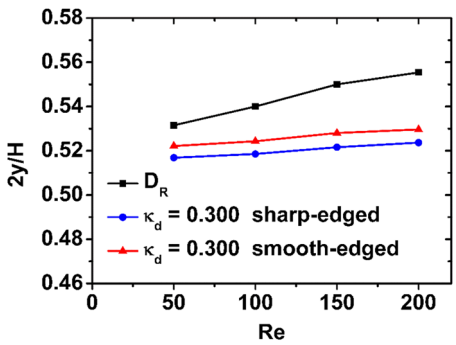

FIG. 12. The variation of equilibrium position of disk-like particles with κ_d = 0.3 in a channel with W/H = 1. Two types of disk-like particles, sharp-edged and smooth-edged, are simulated.

Figure 14 shows the distribution of surface stresses of the RBC-like particle constrained at (0.6, 0) under Re = 100. The RBC-like particle is rolling counterclockwise with a constant angular velocity. By viewing the surface stresses in different perspectives, the large stresses are found to mainly appear in the top, bottom-left, and bottom-right of the particle surface. The top surface near the wall has the largest surface stresses. The corresponding force vectors are along the flow direction and dominated by the shear-induced viscous stress. Surface stresses on the left surface facing the flow contribute a lift directing to the wall, while surface stresses on the right side push the particle away from the wall. The stresses on the top and bottom surfaces tend to drive the particle to roll counterclockwise, while the stresses on the left and right surface have the opposite effect. The stresses balance themselves in the circumferential direction. The circumferential surface of the RBC-like particle is observed to be squeezed and stretched in the directions with about $\pi/4$ and $3\pi/4$ to the x-axis, respectively. The different parts of circumferential

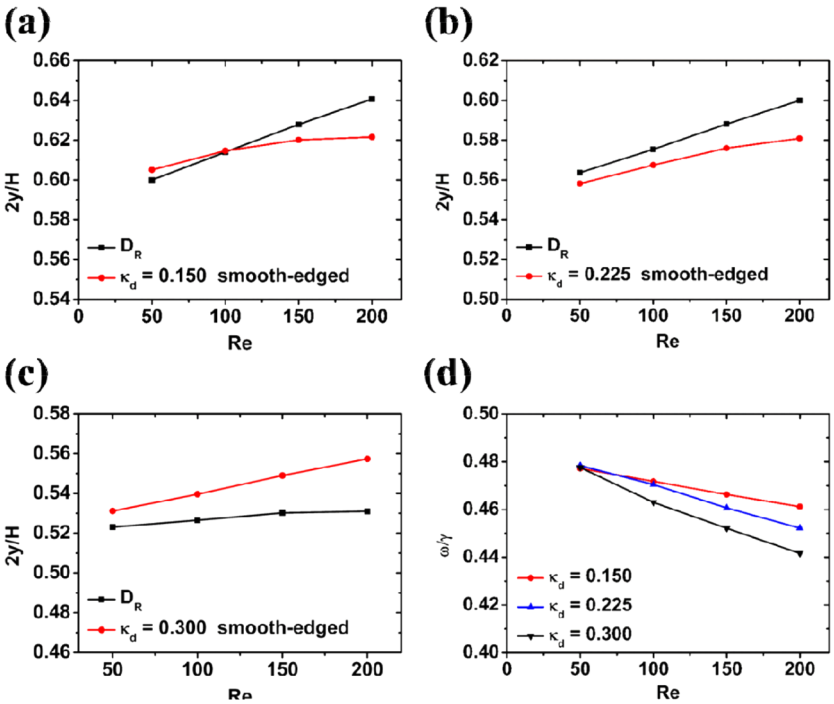

FIG. 13. The influence of the blockage ratio of smooth-edged disk-like particles with 7.5 μm in diameter and 2 μm in thickness in a channel with $W/H = 1$: (a) $\kappa_d = 0.150$, (b) $\kappa_d = 0.225$, and (c) $\kappa_d = 0.300$. (d) The variation of angular velocity of smooth-edged disk-like particles located at (0.5, 0) is shown for different κ_d.

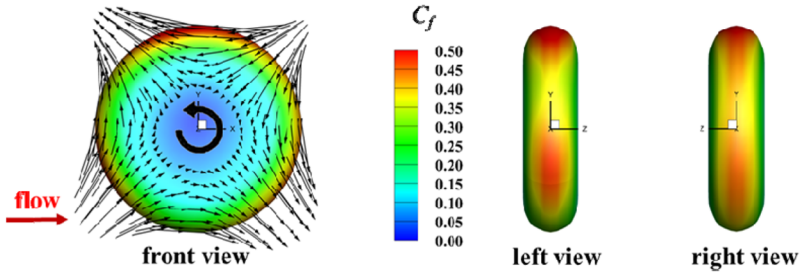

FIG. 14. The distribution of C_f for a RBC-like particle with $\kappa_d = 0.150$ located at (0.6, 0) under Re = 100 is shown with contour plots. The contours denote the absolute value and the vectors denote the orientation.

surface continuously roll through these two directions, which may be helpful for investigation of the shape stability of the RBCs.[42]

IV. CONCLUSION

In the present work, we conduct three-dimensional direct numerical simulations to investigate the inertial migrations of cylindrical particles in rectangular microchannels under different aspect ratios, blockage ratios, channel aspect ratios, and Reynolds numbers. Our results show that the lift and the torque experienced by cylindrical particles vary periodically over each half rotation cycle of the particles. Extreme values of the lift are observed when diagonal lines of the particle cross section in the x-y plane are nearly perpendicular to the wall. Distributions of surface stresses demonstrate that the surface stresses on the particle end near the wall play important roles in the particle rotation. The measurements of lift forces for particles with $\kappa = 0.3$ indicate that there are four stable equilibrium positions for the channel with $W/H = 1$ under Re varying from 50 to 400, while the number for the channel with $W/H = 2$ increases from two (Re = 50, 100) to four (Re = 200, 300, 400). Inertial migrations of spherical particles with three types of diameters are also carried out to investigate the equivalent diameters of cylindrical particles. Equivalent diameters are found to monotonously increase with Re for both long cylindrical particles ($L/D > 1$) and short cylindrical particles ($L/D < 1$), regardless of the change of κ. Complicated variations of equilibrium positions under Re varies from 50 to 200 are also addressed in details. In a square channel, the equilibrium positions of cylindrical particles mainly shift to the wall with increasing Re, though showing smoother change compared with spherical particles with rotational diameters, D_R, as diameters. However, the remarkable shift away from the wall is observed under Re varying from 50 to 200 in a rectangular channel with $W/H = 2$ for the cylindrical particle with $L/D = 2$ and $\kappa = 0.3$. The RBC-like particles with $L/D = 4{:}15$ are also investigated as short cylindrical particles. By investigating the surface stresses on the RBC-like particle, we find that its circumferential surface is squeezed and stretched in the directions with about $\pi/4$ and $3\pi/4$ to the x-axis, respectively. Our simulations systematically investigate the inertial migration of cylindrical particles, revealing their typical migration behavior and the relationship and difference with spherical particles. The findings may be helpful for the precise manipulation of cylinder-like particles and provide a reference for the study of other non-spherical particles.

ACKNOWLEDGMENTS

This work was supported financially by the National Natural Science Foundation of China (NSFC) (Grant Nos. 11572334, 11402274, and 11772343), the CAS Strategic Priority Research Program (No. XDB22040403), and the CAS Key Research Program of Frontier Sciences (No. QYZDB-SSW-JSC036).

[1] Y. Ai, A. Beskok, D. T. Gauthier, S. W. Joo, and S. Qian, "Dc electrokinetic transport of cylindrical cells in straight microchannels," Biomicrofluidics **3**, 44110 (2009).
[2] N. Lewpiriyawong, C. Yang, and Y. C. Lam, "Continuous sorting and separation of microparticles by size using AC dielectrophoresis in a PDMS microfluidic device with 3-D conducting PDMS composite electrodes," Electrophoresis **31**, 2622 (2010).
[3] X. Chen, Y. Ren, W. Liu, X. Feng, Y. Jia, Y. Tao, and H. Jiang, "A simplified microfluidic device for particle separation with two consecutive steps: Induced charge electro-osmotic prefocusing and dielectrophoretic separation," Anal. Chem. **89**, 9583 (2017).
[4] P. Li, Z. Mao, Z. Peng, L. Zhou, Y. Chen, P. H. Huang, C. I. Truica, J. J. Drabick, W. S. El-Deiry, M. Dao, S. Suresh, and T. J. Huang, "Acoustic separation of circulating tumor cells," Proc. Natl. Acad. Sci. U. S. A. **112**, 4970 (2015).
[5] G. Nava, F. Bragheri, T. Yang, P. Minzioni, R. Osellame, I. Cristiani, and K. Berg-Sørensen, "All-silica microfluidic optical stretcher with acoustophoretic prefocusing," Microfluid. Nanofluid. **19**, 837 (2015).
[6] N. Xia, T. P. Hunt, B. T. Mayers, E. Alsberg, G. M. Whitesides, R. M. Westervelt, and D. E. Ingber, "Combined microfluidic-micromagnetic separation of living cells in continuous flow," Biomed. Microdevices **8**, 299 (2006).
[7] L. Liang, C. Zhang, and X. Xuan, "Enhanced separation of magnetic and diamagnetic particles in a dilute ferrofluid," Appl. Phys. Lett. **102**, 234101 (2013).
[8] D. Vigolo, R. Rusconi, H. A. Stone, and R. Piazza, "Thermophoresis: Microfluidics characterization and separation," Soft Matter **6**, 3489 (2010).
[9] Y. Zhao, C. Zhao, J. He, Y. Zhou, and C. Yang, "Collective effects on thermophoresis of colloids: A microfluidic study within the framework of DLVO theory," Soft Matter **9**, 7726 (2013).
[10] A. J. Chung, D. R. Gossett, and D. Di Carlo, "Three dimensional, sheathless, and high-throughput microparticle inertial focusing through geometry-induced secondary flows," Small **9**, 685 (2013).
[11] J. Oakey, R. W. Applegate, Jr., E. Arellano, D. Di Carlo, S. W. Graves, and M. Toner, "Particle focusing in staged inertial microfluidic devices for flow cytometry," Anal. Chem. **82**, 3862 (2010).
[12] A. J. Chung, D. Pulido, J. C. Oka, H. Amini, M. Masaeli, and D. Di Carlo, "Microstructure-induced helical vortices allow single-stream and long-term inertial focusing," Lab Chip **13**, 2942 (2013).
[13] A. E. Reece and J. Oakey, "Long-range forces affecting equilibrium inertial focusing behavior in straight high aspect ratio microfluidic channels," Phys. Fluids **28**, 043303 (2016).
[14] A. A. S. Bhagat, H. W. Hou, L. D. Li, C. T. Lim, and J. Han, "Pinched flow coupled shear-modulated inertial microfluidics for high-throughput rare blood cell separation," Lab Chip **11**, 1870 (2011).
[15] C. Liu, G. Hu, X. Jiang, and J. Sun, "Inertial focusing of spherical particles in rectangular microchannels over a wide range of Reynolds numbers," Lab Chip **15**, 1168 (2015).
[16] J. S. Sun, M. M. Li, C. Liu, Y. Zhang, D. B. Liu, W. W. Liu, G. Q. Hu, and X. Y. Jiang, "Double spiral microchannel for label-free tumor cell separation and enrichment," Lab Chip **12**, 3952 (2012).
[17] J. Zhou, P. V. Giridhar, S. Kasper, and I. Papautsky, "Modulation of aspect ratio for complete separation in an inertial microfluidic channel," Lab Chip **13**, 1919 (2013).
[18] J. Zhou and I. Papautsky, "Fundamentals of inertial focusing in microchannels," Lab Chip **13**, 1121 (2013).
[19] A. J. Mach and D. Di Carlo, "Continuous scalable blood filtration device using inertial microfluidics," Biotechnol. Bioeng. **107**, 302 (2010).
[20] S. C. Hur, N. K. Henderson-MacLennan, E. R. B. McCabe, and D. Di Carlo, "Deformability-based cell classification and enrichment using inertial microfluidics," Lab Chip **11**, 912 (2011).
[21] J. S. Dudani, D. R. Gossett, H. T. K. Tse, and D. Di Carlo, "Pinched-flow hydrodynamic stretching of single-cells," Lab Chip **13**, 3728 (2013).
[22] D. R. Gossett, H. T. K. Tse, J. S. Dudani, K. Goda, T. A. Woods, S. W. Graves, and D. Di Carlo, "Inertial manipulation and transfer of microparticles across laminar fluid streams," Small **8**, 2757 (2012).
[23] G. Segre and A. Silberberg, "Radial particle displacements in Poiseuille flow of suspensions," Nature **189**, 209 (1961).
[24] P. G. Saffman, "The lift on a small sphere in a slow shear flow," J. Fluid Mech. **22**, 385 (1965).
[25] B. P. Ho and L. G. Leal, "Inertial migration of rigid spheres in two-dimensional unidirectional flows," J. Fluid Mech. **65**, 365 (1974).
[26] J. A. Schonberg and E. J. Hinch, "Inertial migration of a sphere in Poiseuille flow," J. Fluid Mech. **203**, 517 (2006).
[27] E. S. Asmolov, "The inertial lift on a spherical particle in a plane Poiseuille flow at large channel Reynolds number," J. Fluid Mech. **381**, 63 (1999).
[28] D. Di Carlo, J. F. Edd, K. J. Humphry, H. A. Stone, and M. Toner, "Particle segregation and dynamics in confined flows," Phys. Rev. Lett. **102**, 094503 (2009).
[29] H. Shichi, H. Yamashita, J. Seki, T. Itano, and M. Sugihara-Seki, "Inertial migration regimes of spherical particles suspended in square tube flows," Phys. Rev. Fluids **2**, 044201 (2017).
[30] Y.-S. Choi, K.-W. Seo, and S.-J. Lee, "Lateral and cross-lateral focusing of spherical particles in a square microchannel," Lab Chip **11**, 460 (2011).
[31] M. Abbas, P. Magaud, Y. Gao, and S. Geoffroy, "Migration of finite sized particles in a laminar square channel flow from low to high Reynolds numbers," Phys. Fluids **26**, 123301 (2014).
[32] Y.-S. Choi and S.-J. Lee, "Holographic analysis of three-dimensional inertial migration of spherical particles in micro-scale pipe flow," Microfluid. Nanofluid. **9**, 819 (2010).
[33] N. Nakagawa, T. Yabu, R. Otomo, A. Kase, M. Makino, T. Itano, and M. Sugihara-Seki, "Inertial migration of a spherical particle in laminar square channel flows from low to high Reynolds numbers," J. Fluid Mech. **779**, 776 (2015).
[34] S. C. Hur, S.-E. Choi, S. Kwon, and D. D. Carlo, "Inertial focusing of non-spherical microparticles," Appl. Phys. Lett. **99**, 044101 (2011).
[35] M. Masaeli, E. Sollier, H. Amini, W. Mao, K. Camacho, N. Doshi, S. Mitragotri, A. Alexeev, and D. Di Carlo, "Continuous inertial focusing and separation of particles by shape," Phys. Rev. X **2**, 031017 (2012).
[36] H. Amini, W. Lee, and D. Di Carlo, "Inertial microfluidic physics," Lab Chip **14**, 2739 (2014).
[37] S.-D. Chen, T.-W. Pan, and C.-C. Chang, "The motion of a single and multiple neutrally buoyant elliptical cylinders in plane Poiseuille flow," Phys. Fluids **24**, 103302 (2012).
[38] I. Lashgari, M. N. Ardekani, I. Banerjee, A. Russom, and L. Brandt, "Inertial migration of spherical and oblate particles in straight ducts," J. Fluid Mech. **819**, 540 (2017).
[39] S.-L. Huang, S.-D. Chen, T.-W. Pan, C.-C. Chang, and C.-C. Chu, "The motion of a neutrally buoyant particle of an elliptic shape in two dimensional shear flow: A numerical study," Phys. Fluids **27**, 083303 (2015).
[40] T. Inamuro, K. Maeba, and F. Ogino, "Flow between parallel walls containing the lines of neutrally buoyant circular cylinders," Int. J. Multiphase Flow **26**, 1981 (2000).
[41] T.-W. Pan and R. Glowinski, "Direct simulation of the motion of neutrally buoyant circular cylinders in plane Poiseuille flow," J. Comput. Phys. **181**, 260 (2002).
[42] D. Di Carlo, D. Irimia, R. G. Tompkins, and M. Toner, "Continuous inertial focusing, ordering, and separation of particles in microchannels," Proc. Natl. Acad. Sci. U. S. A. **104**, 18892 (2007).
[43] M. Li, H. E. Muñoz, A. Schmidt, B. Guo, C. Lei, K. Goda, and D. Di Carlo, "Inertial focusing of ellipsoidal *Euglena gracilis* cells in a stepped microchannel," Lab Chip **16**, 4458 (2016).
[44] J. Zhang, S. Yan, D. Yuan, G. Alici, N.-T. Nguyen, M. Ebrahimi Warkiani, and W. Li, "Fundamentals and applications of inertial microfluidics: A review," Lab Chip **16**, 10 (2016).
[45] Q. M. Tan, *Dimensional Analysis: With Case Studies in Mechanics* (Springer-Verlag, Berlin, Heidelberg, 2011).
[46] D. L. Brown, W. D. Henshaw, and D. J. Quinlan, "Overture: An object-oriented framework for solving partial differential equations," in *Scientific Computing in Object-Oriented Parallel Environments* (Springer, Berlin, Heidelberg, 1997), p. 177.
[47] H. Bruus, *Theoretical Microfluidics* (Oxford University Press, Oxford, 2007).

[48]W. D. Henshaw, "A fourth-order accurate method for the incompressible Navier-Stokes equations on overlapping grids," J. Comput. Phys. **113**, 13 (1994).
[49]P. F. W. D. Henshaw, "Oges user guide, version 1.0, a solver for steady state boundary value problems on overlapping grids," Technical Report No. LA-UR-96-3468, Los Alamos National Laboratory, 1998.
[50]C. Liu, C. D. Xue, J. S. Sun, and G. Q. Hu, "A generalized formula for inertial lift on a sphere in microchannels," Lab Chip **16**, 884 (2016).
[51]X. Chen, C. Xue, L. Zhang, G. Hu, X. Jiang, and J. Sun, "Inertial migration of deformable droplets in a microchannel," Phys. Fluids **26**, 112003 (2014).
[52]A. A. S. Bhagat, S. S. Kuntaegowdanahalli, and I. Papautsky, "Enhanced particle filtration in straight microchannels using shear-modulated inertial migration," Phys. Fluids **20**, 101702 (2008).
[53]J. Feng, H. H. Hu, and D. D. Joseph, "Direct simulation of initial value problems for the motion of solid bodies in a Newtonian fluid. Part 2. Couette and Poiseuille flows," J. Fluid Mech. **277**, 271 (1994).
[54]G. B. Jeffery, "The motion of ellipsoidal particles in a viscous fluid," Proc. R. Soc. A **102**, 161 (1922).
[55]D. Qi and L. Luo, "Transitions in rotations of a nonspherical particle in a three-dimensional moderate Reynolds number Couette flow," Phys. Fluids **14**, 4440 (2002).
[56]H. Schmidschonbein and R. Wells, "Fluid drop-like transition of erythrocytes under shear," Science **165**, 288 (1969).
[57]T. M. Fischer, M. Stohrliesen, and H. Schmidschonbein, "The red cell as a fluid droplet: Tank tread-like motion of the human erythrocyte membrane in shear flow," Science **202**, 894 (1978).
[58]D. Cordasco, A. Yazdani, and P. Bagchi, "Comparison of erythrocyte dynamics in shear flow under different stress-free configurations," Phys. Fluids **26**, 041902 (2014).
[59]J. Dupire, M. Socol, and A. Viallat, "Full dynamics of a red blood cell in shear flow," Proc. Natl. Acad. Sci. U. S. A. **109**, 20808 (2012).
[60]K. Sinha and M. D. Graham, "Dynamics of a single red blood cell in simple shear flow," Phys. Rev. E **92**, 042710 (2015).